ACS APPLIED MATERIALS & INTERFACES

www.acsami.org

Research Article

Reversible and Programmable Wettability of Laser-Induced Graphene Papers via *In Situ* Joule Heating-Triggered Superslippery Surfaces

Yanan Wang,[‖] Pingping Hao,[‖] Sida Luo,* Yan Gao, Mingguang Han,* Mengchen Sun, and Xiao Wu*

Cite This: https://doi.org/10.1021/acsami.5c04045

Read Online

ACCESS | Metrics & More | Article Recommendations | Supporting Information

ABSTRACT: Reversible surface materials with programmable wettability play an increasingly vital role in a wide variety of fields from science to industry. Based on laser-induced graphene (LIG) technology, we innovatively propose a paraffin-infused porous LIG paper (P-LIGP) with tunable superslippery wettability. On account of graphene's excellent electrical property, paraffin in P-LIGP can transit rapidly from a solid-to-liquid state in response to the *in situ* Joule heating effect. Thus, a LIGP surface is created with a dynamic and reversible transition between slippery and nonslippery state. In addition, combining the patternable performance with tunable LIGP resistance, the paraffin layer from P-LIGP can be selectively melted based on Ohm's law and Kirchhoff's laws, thus enabling special flow pathways with programmable wettability for manipulating the droplets with various straight/oblique/arc/S-shaped sliding patterns. These applications with customizable LIG resistance performance promise the *in situ* Joule heating of P-LIGP for designing intelligent and flexible temperature-responsive surfaces.

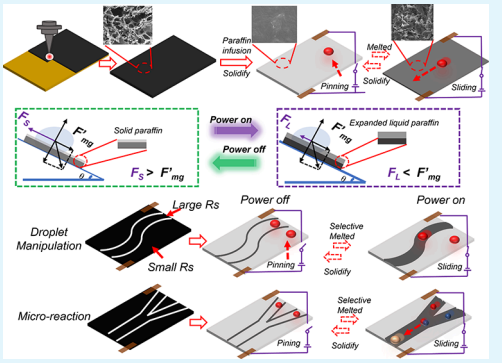

KEYWORDS: *laser-induced graphene, superslippery surface, graphene papers, programmable wettability, Joule heating*

1. INTRODUCTION

With rapid progress of advanced technologies and the emergence of multifunctional surface materials, surfaces with unique wettability (e.g., superhydrophilic, superhydrophobic, superolephilic, and superolephobic characteristics) have garnered great research interest due to their potential value in our daily life and industrial areas. Among those surfaces with special wettability, superslippery liquid-infused porous surfaces (SLIPS) inspired from the pitcher plant have received more attention and been widely applied in various fields, including microfluidic,[1] self-cleaning,[2,3] antifouling,[4,5] anticorrosion,[6,7] anti-icing,[8,9] and droplet manipulation systems.[10] In addition, SLIPS- related works also provide application value in medical health monitoring,[11] human computer interaction,[12] flexible sensors,[13] self-healing actuators,[14] and other related fields.[15] However, most reported SLIPS only satisfy the demands to the fixed environment and are unable to achieve reversible wettability at certain temperature, force, light, and so on. Recently, SLIPS which could respond to single[16] or multiple external stimuli[17,18] (e.g., electric field, magnetic field, stress, temperature, and light) to realize reversible wettability based on responsive substrates, lubricants, and repellent liquids have attracted notable attention. Although chemical modification,[19] spray coating,[20] sol−gel,[21] layer-by-layer deposition,[22] and laser ablation[23,24] have been widely used for fabricating and assembling the responsive SLIPS, with patterned or tunable wettability, the above methods require complicated processes[25] and expensive reagents.[26] Accordingly, the prepared SLIPS still exhibit lower switch efficiency, nonprogrammable wettability, and stimulus dependency, restricting their applications in diversified fields.

As an emerging carbon-based material, porous graphene and its derivatives have been extensively studied for assembling multifunctional structures[27] and devices[28,29] due to the excellent performance of photothermal conversion,[30] wettability regulation,[31,32] moisture response, and mechanical robustness, as well as simple and customizable fabrication methods.[33,34] As a key structural format, graphene films have been successfully used for external stress or light-induced SLIPS fabrication and have realized programmable wettability and shape-memory wettability with lower sliding angle and high liquid repellency.[35,36] However, general problems of film preparation, including multisteps, time-consuming, complex raw materials, and limited selection of substrates, still exist for hindering the wide applications of graphene film on superslippery surfaces.

Received: February 26, 2025
Revised: March 27, 2025
Accepted: March 29, 2025

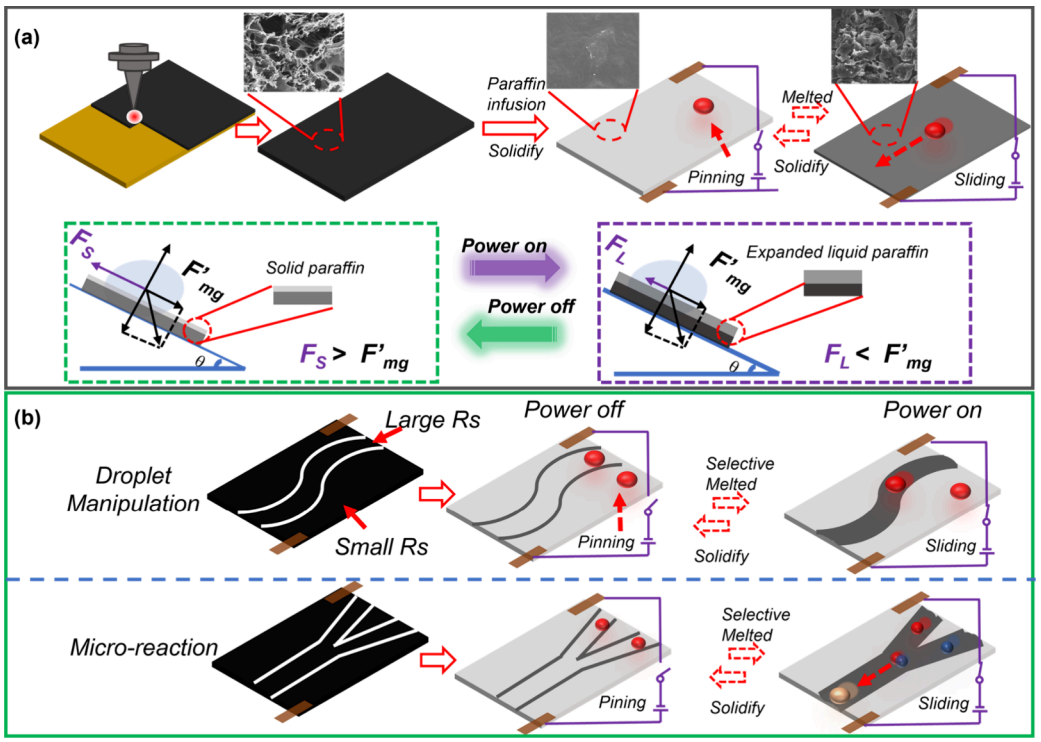

Figure 1. Schematic diagram of the P-LIGP with designable and tunable wettability. (a) Preparation of paraffin infused LIGPs with reversible surface wettability and the mechanical analysis of droplet during nonslippery or slippery state. (b) Joule heating-controlled local melting pathways on the surface of P-LIGP for controllable droplet manipulation.

To alleviate the above issues, laser-induced graphene (LIG) relies on the photothermal energy of a specialized laser (e.g., CO_2 laser) to locally heat the surface of certain polymeric precursors (e.g., polyimide) to form porous graphene structures through pyrolysis and carbonization. The synthesis method of LIG is simple and efficient and can be directly patterned on a flexible substrate, which is suitable for large-scale production. As demonstrated in our previous studies, LIG papers (LIGPs)[37] with tunable microstructures and properties were prepared based on the unique one-step laser scribing process with the aid of computer design, thus reflecting unique assembling advantages in terms of ease-of-operation, high production efficiency, and scalable dimension for applications, ranging from sensors,[38] heaters,[39] and antibiofouling interfaces.[40] At present, LIG, as a superlubricated surface, can be used in relevant applications such as anti-ice, antipollution, and anticorrosion, as well as seawater desalination,[41] oil−water separation,[42] and photocatalytic degradation of pollutants.[43] In addition, the highly efficient Joule heating characteristics of LIGP could further support material synthesis, morphology control, and functional performance through the current-heat conversion mechanism. For example, Ye et al. successfully repair defects in LIG through the flash joule heating (FJH) process by significantly improving its electrical conductivity and crystallinity.[44]

In this paper, we innovatively present paraffin-infused porous LIGP (P-LIGP) with designable and programmable wettability through *in situ* Joule heating-triggered droplet manipulation. Benefiting from uniform porous structures combined with the highly efficient Joule heating property, the structure of P-LIGP stays stable under high current-heat energy when compared with other *ex situ* heat sources,[45,46] while exhibiting smaller sliding angles based on smaller surface roughness and larger specific surface area. Moreover, by tuning the laser-power controlled resistance patterns followed by Ohm's law and Kirchhoff's laws, we could program the surface wettability of P-LIGP by selectively melting the paraffin layer toward the realization of droplet manipulation and micro-chemical reactions. More importantly, the highly efficient Joule heating characteristic could further promise the ability of P-LIGP for manipulating droplets with rapid and shifting motions between sliding and pinning on 2D/3D surfaces. Significantly, the scratched P-LIGP can be self-healed within 10 s under the assistance of Joule heat. Owing to intelligent temperature response, dynamic reversible wettability regulation, and programmable wettability path design from P-LIGP technology, it is highly anticipated that the proposed P-LIGP has shown great potentiality for designing and manufacturing next-generation smart devices.

2. EXPERIMENTAL SECTION

2.1. Preparation of LIGPs. Laser-induced graphene papers (LIGP) were produced by a 10.6 μm CO_2 laser platform (DLS 2.3, Universal Laser Systems, Inc.), and polyimide fibrous paper (PI paper) was used as the carbon source precursor. The detailed processing windows are as follows: the line space, scan rate, and pulse resolution were fixed at 100 μm, 50.8 mm/s, and 500 pixels per inch, respectively. With the laser power ranging from 0.75 to 2.0 W, all the samples were processed under vector mode of the laser platform. For patterned LIGPs, patterns with higher resistance were processed at a lower power, and the rest of the areas were processed at a higher power to ensure a large temperature difference for accurate and selective paraffin melting. All the patterns were drawn by CorelDraw software.

2.2. Fabrication of P-LIGPs. The electrodes were prepared by coating silver paste on both sides of LIGPs first, and then were packaged by copper foil. Solid paraffin as the infused oil was purchased from the Aladdin group with the melting point of 56−58

https://doi.org/10.1021/acsami.5c04045
ACS Appl. Mater. Interfaces XXXX, XXX, XXX−XXX

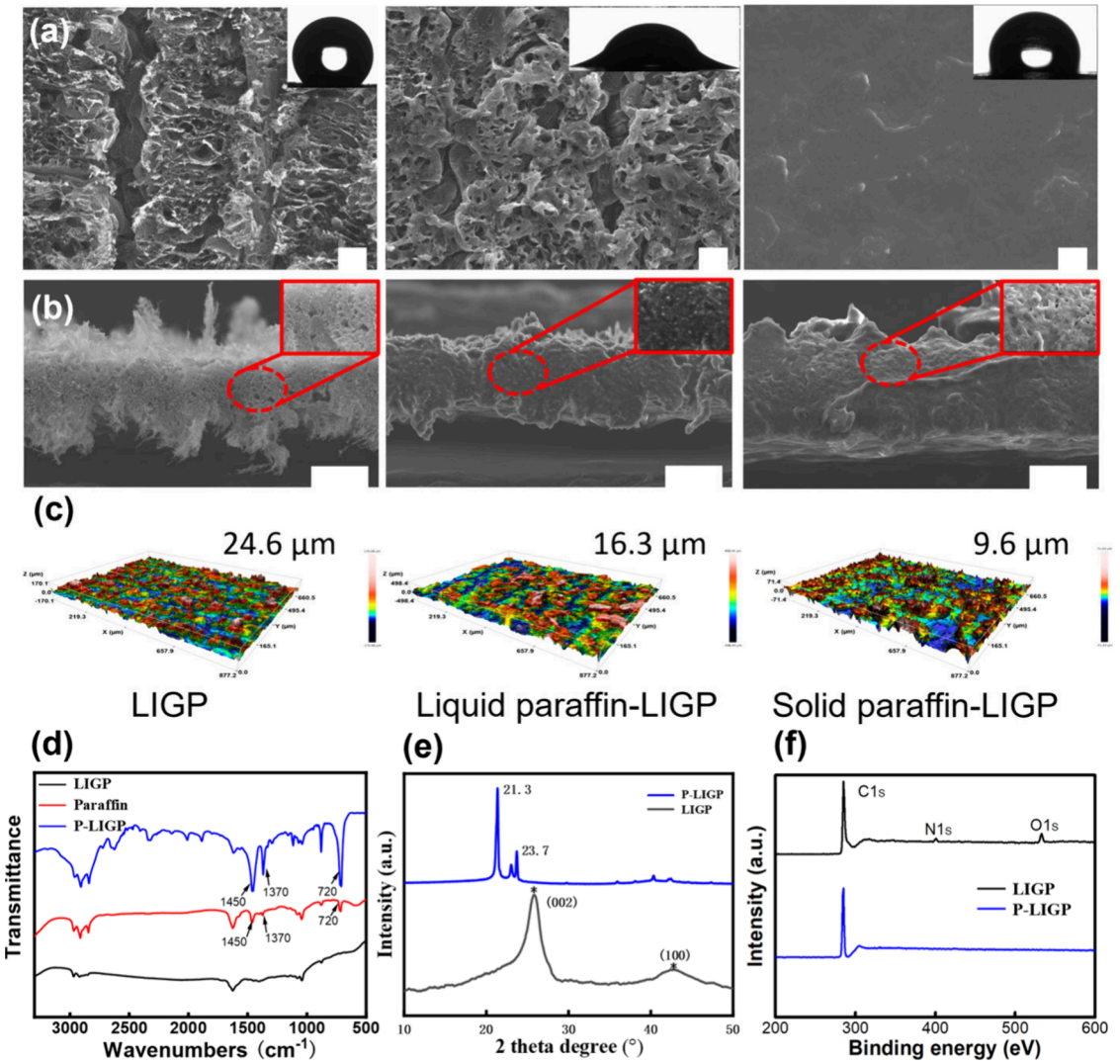

Figure 2. Structural characterizations of LIGPs. (a) SEM images from the surface of LIGP, liquid paraffin-covered LIGP, and P-LIGP with their surface wettability. The white scale bars represent 100 μm. (b) Cross-sectional SEM images of LIGPs. The white scale bars represent 100 μm. (c) 3D confocal microscope pictures of LIGPs. (d) FT-IR spectra of paraffin and LIGPs. (e) XRD pattern of paraffin and LIGPs. (f) XPS full-scan spectrum of C 1s and O 1s of paraffin and LIGPs.

°C. For the solid paraffin-infused LIGPs, the melting paraffin was dropped on the LIGP surface by using a pipet to cover the whole LIGP surface to form the paraffin film.

2.3. Preparation of Patterned P-LIGPs. Different patterns were drawn in advance with CorelDraw using different combinations of laser power conditions to obtain LIGPs with different surficial resistance distributions. Subsequently, the phase change LIGP composites were prepared following the same parrafin coating process. When the width of heating path was set at least at 5 mm, the temperature required for paraffin melting could be reached, so the width of relevant tests in the experiment was kept at 5 mm, as shown in Figure S4.

2.4. Characterizations of P-LIGPs. Scanning electron microscopy (SEM) images were obtained using a JEOL JSM 7001F. A digital camera Canon 5D Mark II was responsible for capturing photos and videos. A Horiba HR800 Raman microscope, with the 532 nm excitation laser, was used to obtain Raman spectra. Specific surface area was measured and calculated by using a Brunauer–Emmette–Teller (BET) analyzer (Autosorb-iQ-MP, Quan-tachrome Instruments). An ESCALAB 250Xi equipped with a 200 μm X-ray microprobe was used for X-ray photoelectron spectroscopy (XPS) characterization. Fourier transform infrared (FTIR) spectroscopy was performed with a NICOLET 6700 FTIR apparatus (Thermo Scientific, USA). A Keithley 2450 Source meter, interfaced with a LabVIEW program, was applied for sheet resistance and conductivity measurements. The real-time temperature monitoring process was carried out by locally embedding an Omega K type thermocouple and collected by a LabVIEW programmed Keithley 7510 multimeter. A FLIR T420 IR camera was also responsible for capturing infrared videos or images of P-LIGP. The temperature variation was recorded, and the average temperature was determined. A constant direct current (DC) voltage was applied to control the electro-induced superslippery behaviors of P-LIGPs.

2.5. Lubricating Performance Evaluations of P-LIGP. WCA (water contact angle) and WSA (water sliding angle) were measured by an OCA20 instrument (Data-Physics, Stuttgart, Germany), and the average WCA values were calculated for at least four different locations with the liquid volume of 4 μL at room temperature. The durability of P-LIGPs was evaluated by exploring 120 heating cyclic tests based on *in situ* Joule heating, and the mechanical stability was further assessed by bending, stretching, and rolling P-LIGP specimens, performed on E44.104 mechanical analyzer. The paraffin storage ability of P-LIGP was evaluated by using a spin coater rotated at different speeds.

https://doi.org/10.1021/acsami.5c04045
ACS Appl. Mater. Interfaces XXXX, XXX, XXX−XXX

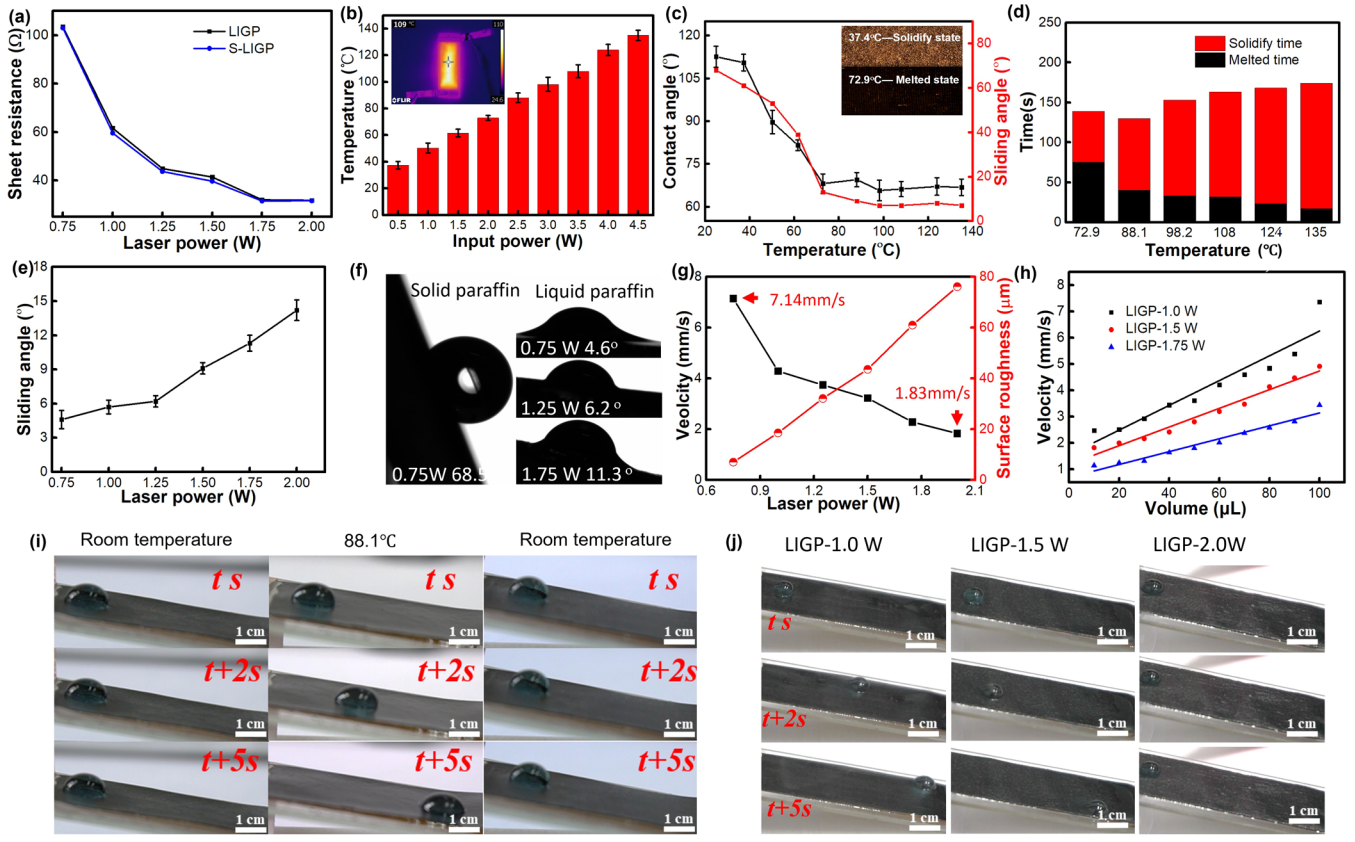

Figure 3. Electrical and electrothermal properties of LIGPs and effects of microstructures on lubrication properties. (a) Sheet resistance of LIGPs/P-LIGPs made at various laser powers. (b) The relationship between surfaces saturated temperature of LIGPs and different input powers. (c) WCA and WSA with the variation of temperatures; inset images are the dynamic process of paraffin from solidification to melted state. (d) Comparison of melted and resolidified time of paraffin under different temperatures. (e) WCA and WSA with the variation of laser powers. (f) Tested pictures of water WCA and WSA on LIGPs surface. (g) Moving velocity of 50 μL water droplet on LIGP surface with various surface roughness (title angle = 10°, temperature = 88.2 °C). (h) Moving velocity with the variation of liquid volume on P-LIGP-1.0 W surface (title angle = 10°, temperature = 88.2 °C). (j) The wettability dynamic control for 30 μL droplet sliding down the surface of the LIGP at a 10° gradient. (i) The wettability dynamic control for 30 μL droplet sliding down the surface of the various LIGP surface fabricated under different laser power.

3. RESULTS AND DISCUSSION

3.1. Preparation of P-LIGPs with Diversified Patterned Structures. LIGP with porous structures has promised the excellent *in situ* Joule heating characteristics with stable electrothermal energy transformation.[45] Also, solid paraffin with the temperature-sensitive characteristics has been widely used as phase change materials.[47] Thus, it is interesting to infuse the porous LIGP with a solid paraffin layer to realize *in situ* Joule heating triggered surficial phase transitions for promising the reversible superslippery performance. Figure 1 reveals the combination strategy of the novel LIGP processing and temperature-controlled paraffin layer coating to form the P-LIGP surface with programmed superslippery property. Figure 1a shows the detailed fabrication process. The reversible process of P-LIGP from nonslippery to slippery could be achieved when the covered paraffin layer changes from solid to melted state. It is clear that the paraffin could reversibly melt and solidify when the DC source is accordingly turned on or off. For patterned P-LIGPs with selective melting surface, as Figure 1b reveals, various resistance distributions were designed and fabricated by combining different laser power conditions based on Ohm's law and Kirchhoff's laws to realize droplet manipulation. To be specific, areas with larger resistance were processed at 0.75 W, and the laser scribing direction was vertical to the current direction. The rest of areas were processed at 2.0 W to achieve smaller resistance, and the laser scribing direction was parallel to the current direction. According to our previous study, as for series connection

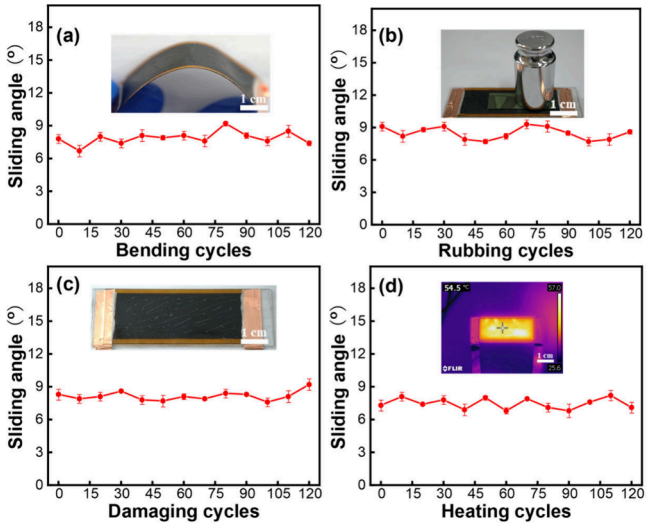

Figure 4. Durability test of the P-LIGP-1.0 W. Variation trend of the WSA with (a) bending cycles, (b) rubbing cycles, (c) damaging cycles, and (d) heating cycles. The tested liquid is deionized water.

https://doi.org/10.1021/acsami.5c04045
ACS Appl. Mater. Interfaces XXXX, XXX, XXX−XXX

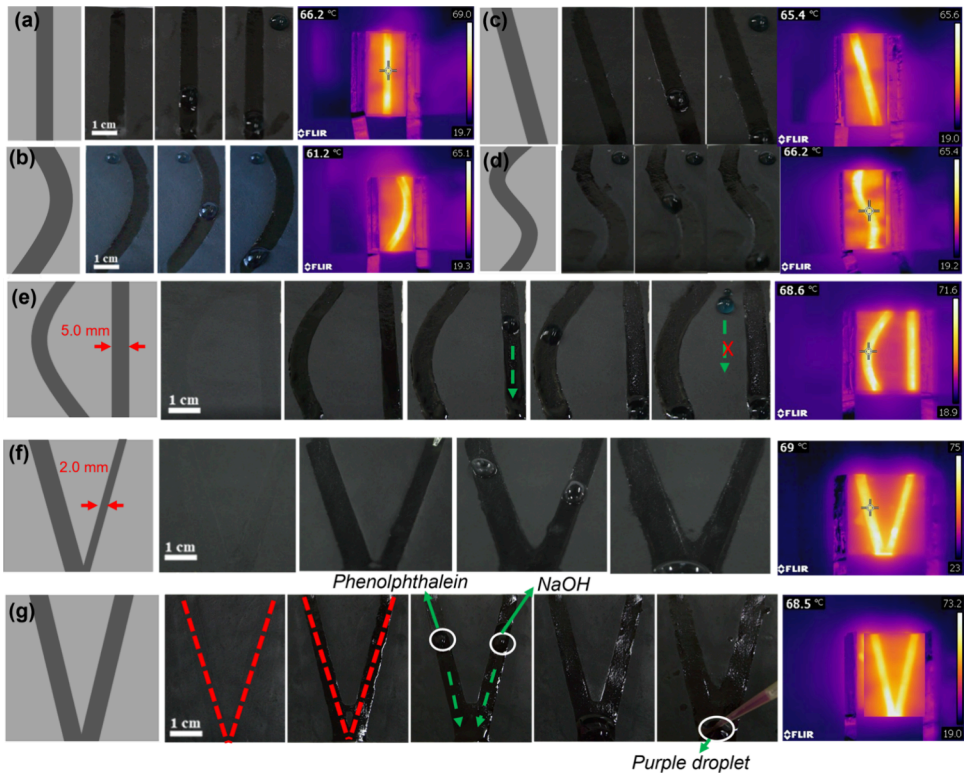

Figure 5. Dynamic control of surface liquid droplet motion guided by design pathways and P-LIGP microfluidics with programmable wetting pathways: (a) straight pathway, (b) oblique pathway, (c) arc pathway, and (d) S-shape pathway. Dynamic control of the droplet movement on P-LIGPs surface guided by (e) straight-arc composite pathways and (f, g) V-shaped pathways for microreaction on specific locations.

circuits, areas with higher resistance could reach higher temperature to selectively melt the covered paraffin film and further program the droplet transport. Accordingly, the programmable process of P-LIGP with unique capability of droplet manipulation could promise potential applications such as microfluidic systems and smart devices.

3.2. Surface Morphology and Surface Chemical Compositions of LIGPs. To compare the difference of LIGPs structures as shown in Figure 2a, the neat LIGP surface was investigated by SEM which exhibited regular line-by-line features and network structures with uniform pore structures. The WCA of the LIGP could maintain 145^o, and the unique porous structures provided sufficient space for paraffin immersion. Liquid paraffin entirely covered and permeated into LIGP porous structures with the aid of capillary forces and strong adhesion forces. Meanwhile, the immersed liquid paraffin connected the pores together, thereby changing the surface into hydrophilic state (WCA ∼ 69.5^o). After the paraffin solidified, all the pores were completely blocked and entirely changed into thin solid paraffin film with amounts of apparent wrinkles, leading to increased WCA ∼110.5. The WCA also reincreased to 110.5^o. The interested changeable phenomenon in the WCA of LIGP was attributed to the variation of surface energy caused by the solid paraffin phase transition. Compared to liquid paraffin-covered LIGP, the P-LIGP surface had a lower surface energy, which resulted in higher WCA.[48] To verify the permeation degree of paraffin, Figure 2b further compares the cross sections of LIGPs, which proved that paraffin completely penetrated and filled LIGP from the end to the top. In addition, a 3D confocal microscope was used to reconstruct the surface morphology of the LIGPs with surface roughness in Figure 2c. The surface roughness values of pure LIGP, liquid paraffin-covered LIGP, and P-LIGP are approximately 24.6, 16.3, and 9.6 μm, respectively, which is corresponded to the SEM images. Additionally, we further conducted the surface chemical composition of LIGPs. As shown in the FT-IR spectra in Figure 2d, the absorption band at 1645 cm^{-1} was ascribed to C═C stretching and bending vibrations of graphene. However, for solid paraffin and P-LIGP, new absorption peaks appeared at 720, 1370, and 1453 cm^{-1} in the spectra, corresponding to the $-(CH_2)_n$, −C−H and −C−O stretching vibration. Furthermore, the XRD pattern of LIGPs is presented in Figure 2e. LIGP exhibits 002 and 100 crystallographic planes at 2θ = 25.8^o and 42.9^o, verifying the interlayer spacing and in-plane structure of graphene. But for P-LIGP, the characteristic strong peaks centered at 2θ = 21.3^o and 23.7^o are attributed to the reflection of (110) and (040) crystallographic planes. Moreover, XPS was further used to compare the variation of the chemical composition of LIGPs. As shown in Figure 2f, peaks for C, N, and O were observed in the XPS spectrum from pure LIGP. For pure LIGP, the element peaks at nearly 284.8, 401.1, and 533.4 eV were contributed to C 1s, O 1s, and N 1s, respectively. While, P-LIGP only exhibited the strong C 1s peak at 284.7 eV, which was ascribed to C−C and C═C bonds from straight-chain alkane of solid paraffin. This phenomenon was ascribed to the fact that the pores in LIGP were fully blocked during the paraffin solidification process so that the graphitic structures were not detected again. The specific surface area of LIGP was also assessed by the nitrogen adsorption and desorption isotherm (Figure S1). It can be observed that the solid paraffin had the smallest specific surface area of 1.23 m^2/g, compared with 4.16 m^2/g of P-LIGP. The results correspond to the blocked porous structures of SEM

https://doi.org/10.1021/acsami.5c04045
ACS Appl. Mater. Interfaces XXXX, XXX, XXX−XXX

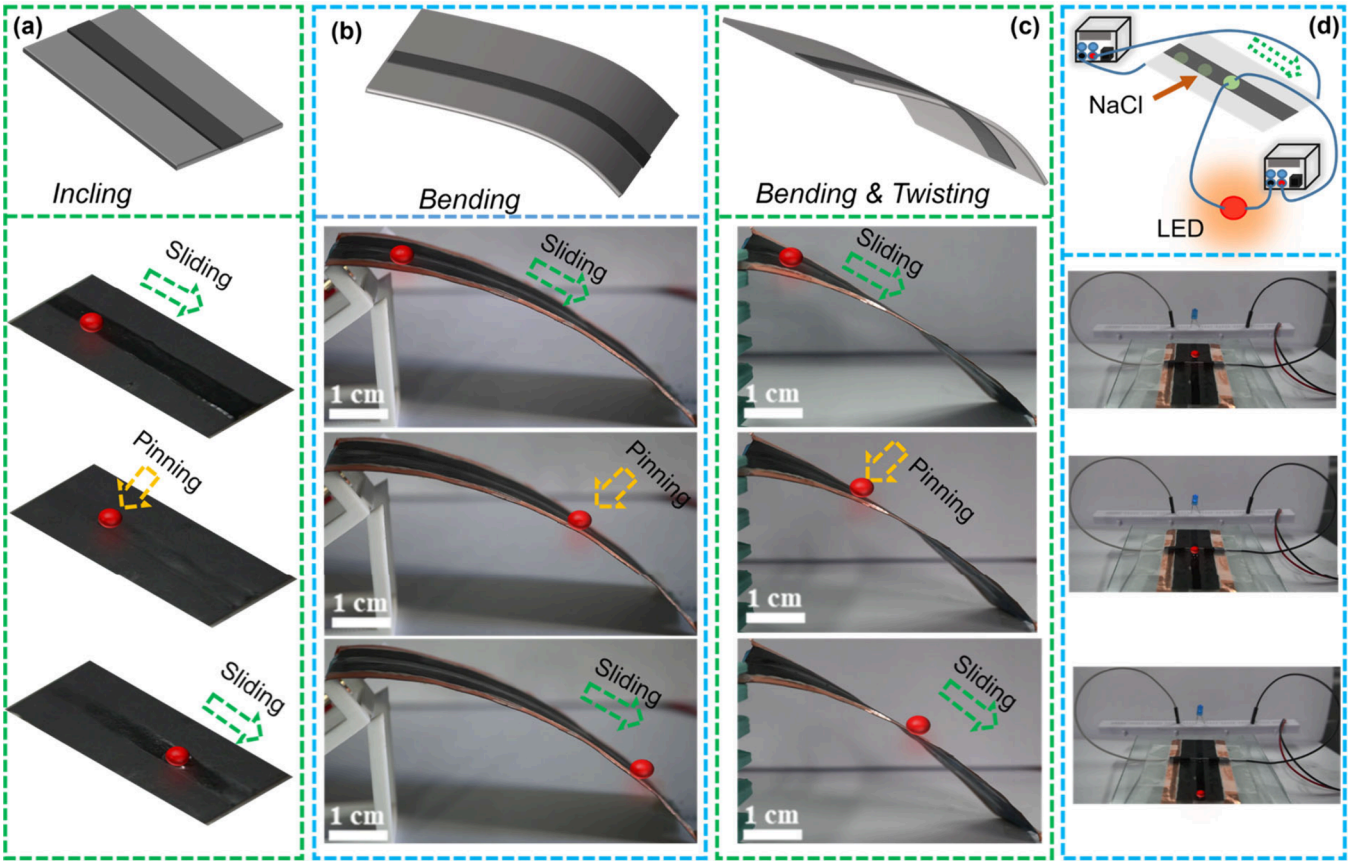

Figure 6. *In-situ* reversible droplet control between pinning and sliding on multidimensional surfaces. (a) Sequential pinning-sliding-pinning motion control of water droplet (~15 μL) on the planar P-LIGP (inclined angle: ~ 10°) by *in situ* loading and unloading the input (applied voltage: 12 V). Water-droplet motion control by *in situ* loading and unloading of Joule heat on (b) curved and (c) twisted P-LIGP surfaces. (d) Home-built electrical circuit incorporated by two power sources, P-LIGP, and saturated NaCl droplet.

images. Oppositely, pure LIGP shows the largest specific surface area of 101.3 m^2/g due to the exposed porous structures. Figure S3 shows the relationship between the processing power and I_D/I_G. In the process of increasing from 0.75W to 2W, I_D/I_G decreases from 0.91 to 0.45, indicating that the defects of graphene composing LIGP are gradually reduced, and the quality of graphene is gradually improved. Based on the discussion above, we further confirmed that the paraffin sufficiently permeated into inner porous structures of LIGP and entirely covered its surface, which laid the foundation for the *in situ* Joule heating-triggered reversible superslippery property.

3.3. Comparison of Switchable Wettability in Different P-LIGPs. Based on the findings in our previous study, combined with the excellent Joule heating characteristic of LIGP, switchable wettability could be available from P-LIGP owing to the phase change of paraffin. Figure 3a first compared the sheet resistance of LIGP and P-LIGP; it is clear that the sheet resistance did not change obviously, which ensured the pristine excellent Joule heating performance of LIGP. Meanwhile, sheet resistance properties also determined the high switch efficiency of the slippery state and nonslippery state. Thus, we first investigated the relationship between input power and surface temperature, as Figure 3b revealed, for a 60 mm × 20 mm P-LIGP-1.0W. The surface temperature enhanced from 37.4 to 135 °C as the input power gradually increased linearly from 0.5 to 4.5 W. Figure 3c compared the wettability of P-LIGP-1.0 W at different surface temperatures. WCA and WSA sharply decreased from 81.6 and 39 to 68.1^o and 13^o when the temperatures were close to the phase change temperature because of the solid-to-liquid transition of the paraffin. Subsequently, the value of WCA and WSA almost maintained consistency when the temperature was higher than the solid paraffin melting point 59 °C. The wettability difference could be attributed to the variable of surface energy in different temperatures. Figure 3c and Video S1 further reveal the dynamic process of paraffin from the solidification state to melted state. Switch efficiency could be considered another important factor in practical applications. So, we further explored the relationship between surface temperature and paraffin melting−solidifying cyclic time. As Figure 3d depicts, with the maximum surface temperature increasing from 72.9 to 135 °C, paraffin melting time gradually decreased from 75 to 17 s, and resolidification time increased from 64 to 157 s, which corresponded to the input power increasing from 0.5 to 4.5 W. Furthermore, we compared the total time including melting and resolidifying time, and the shortest total time was 130 s and appeared at 88.1 °C with the input power of 2.5 W. It could be suggested that higher power also resulted in higher instant temperature, increased heat transfer rate and longer solidification time. Therefore, input power of 2.5 W and surface temperature of 88.2 °C were considered as the optimal parameters for further studies. To demonstrate the programmable wettability feature induced by temperature, we further conducted the verification of wettability dynamic control on the same P-LIGP surface. As presented in Figure 3i and Video

https://doi.org/10.1021/acsami.5c04045
ACS Appl. Mater. Interfaces XXXX, XXX, XXX−XXX

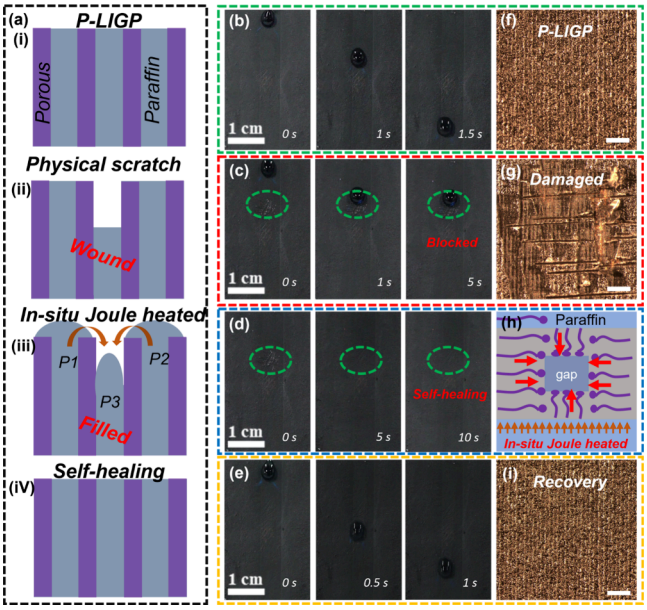

Figure 7. *In situ* self-healing for Joule heat-assisted P-LIGP. (a) Schematic diagram for illustrating the self-healing process of this P-LIGP depending on the capillary effect. (b) Digital pictures for the undamaged P-LIGP with a slippery solid surface, allowing the sliding of a typical water droplet (20 μL) within 1.5 s. (c) Images of the scratched P-LIGP blocking the sliding water droplet. (d) Images of the scratched P-LIGP achieving the self-repairing within 10 s under the assistance of *in situ* Joule heat. (e) Images of the self-healed P-LIGP with a slippery performance comparable or superior to its original surface. Optical microscopic image for the (f) undamaged, (g) scratched, and (i) self-healed P-LIGP. (h) Schematic diagram representing the dynamic self-repairing process by the chemical fusion in the melted paraffin.

S2, P-LIGP-1.0 W was placed on a slope with a tilt angle of 10°; the sliding behavior was monitored and recorded. In detail, the water droplet was pinned on the P-LIGP-1.0 W surface at room temperature (left, Figure 3i), but the droplet would slide down the surface when LIGP was heated at the input power of 2.5 W with surface temperature of 88.2 °C (middle, Figure 3i). After turning off input power to cool down LIGP surface, the droplet would still be pinned on the LIGP surface again (right, Figure 3i). It was indicated that P-LIGP was capable of dynamic and reversible switching wettability depending on the control of the Joule heating effect.

Based on the discussion above, LIGP could absorb paraffin sufficiently and trap it into the unique porous structures, thereby realizing the tunability of the paraffin state switched by Joule heating. Microstructures determining surface roughness play an important role in tuning the superslippery property. Therefore, we further investigated the relationship between surface roughness and the slippery property. Figure 3e compares the WSA of P-LIGPs processed by various laser powers at the temperature of 88.2 °C and tilt angle of 10°. It is clear that with the increasing laser powers from 0.75 to 2.0 W, WSA exhibited the same increased trend. The detailed and real-time WCA and WSA measurements are shown in Figure 3f. Droplet moving velocity was further compared in Figure 3g; for a 50 μL water droplet, moving velocity gradually decreased from 7.14 to 1.83 mm/s with the laser power increased from 0.75 to 2.0 W, which corresponding to the WSA results. We further found that the moving velocity was inversely proportional to the surface roughness, according to the following equation:

$$F_d = F'_{mg} - \mu F_N \quad (1)$$

$$F'_{mg} = mg \sin\theta \quad (2)$$

where F_d is the driven force, θ is the tilt angle, μ is the roughness factor which is proportional to surface roughness, and F_N is the constant for the fixed liquid volume. For LIGP with higher surface roughness, the droplet has greater sliding friction force, but the gravitational component is fixed. Thus, the droplet has a slower moving velocity when the surface roughness increases. For P-LIGP-2.0 W, although there is enough paraffin infused in LIGPs, LIGP with higher surface roughness still hampers the droplet's movement, because the gravitational component is unable to overcome the friction force. Meanwhile, densely and randomly distributed graphene fibers also impede the droplet sliding paths. Furthermore, the relationship between liquid volume and the moving velocity for the P-LIGP-0.75 W was investigated, as Figure 3h revealed; with the liquid volume increasing from 5 to 50 μL, the moving velocity gradually rose from 2.47 to 7.96 mm/s. The reason could be explained by the fact that the gravitational component was proportional to the volume of liquid and provided more power for the sliding process. Images in Figure 3j compare the dynamic sliding process of LIGPs. Therefore, it is clear that droplets on P-LIGP-1.0 W and P-LIGP-1.5 W slide from the top to the end of LIGP quickly after the covered paraffin melted, compared with P-LIGP-1.5 W, where the droplet on P-LIGP-1.0 W had a faster moving velocity in the same time interval. Video S3 also clearly reveals and compares the dynamic sliding process of the droplet on LIGPs surface.

3.4. Durability of P-LIGPs. Stability is an important factor for assessing the in-use property of materials, which will have an enormous effect on large-scale preparations and further applications. Therefore, it is essential to confirm the flexibility and durability of LIGP, which is also a significant research point during their service life. Herein, we evaluated the durability of LIGP in terms of its mechanical and thermal properties. The mechanical properties of the obtained P-LIGPs were measured by varied deformations, including bending, rubbing, and damaging. Heating cyclic tests were used for examining its antifatigue performance. As Figure 4a–c shows, WSAs (<10°) are always consistent even after 120 cyclic bending and stretching damaging tests, which demonstrated the outstanding mechanical and antidamage ability of P-LIGPs. In addition, Figure 4d revealed the heating cyclic test of P-LIGPs; the WSAs almost did not change obviously even after 120 cyclic tests, which exhibited considerable repeatability and consistency. Additionally, the paraffin storage ability of PI paper, a glass slide, and P-LIGPs was further assessed by high shear rate tests. Figure S2a shows the paraffin weight percentage loss at the spin rate 3000 rpm/min for 30 s; the weight loss of PI paper and the glass slide was 89.6% and 73.2%, respectively. P-LIGPs have lost paraffin weight from 28 to 18% with the laser power rising from 0.75 to 2.0 W, far less than PI paper and the glass slide. The reason might be that P-LIGPs could stockpile more paraffin because of the luxuriant porous structures, high specific surface area, and similar chemical properties. But LIGP made at different powers also exhibit a difference in paraffin storage ability. LIGP fabricated under larger power could produce a higher LIG height,[49] which enabled it to retain more paraffin during the shearing

https://doi.org/10.1021/acsami.5c04045
ACS Appl. Mater. Interfaces XXXX, XXX, XXX−XXX

test. Furthermore, the inset image in Figure S2a illustrates the relationship between spin rate and paraffin weight loss, and taking P-LIGP-1.0 W as the sample, the paraffin weight loss increased from 28.1 to 71.3% as the spin rate gradually rose from 1000 to 6000 rpm/min. Figure S2b further revealed that WSA had an obvious increase from 8.8 to 22.1° with the spin rate increasing from 1000 to 6000 rpm/min, which corresponded to paraffin weight loss. The results also illustrated that paraffin plays an essential role in the lubricating property of P-LIGPs. The outstanding mechanical stability and fatigue durability could be summarized by three potential reasons: (i) the strong adhesion force between paraffin film and graphene surface, (ii) the strong molecular force including the hydrogen bond and Vander Waals force, and (iii) filled paraffin continuously released from the unique porous surface structures during the damaged process to refill the destroyed locations.[50] Overall, it was suggested that P-LIGP had a relatively stable superslippery performance during the harsh durability and mechanical tests.

3.5. Patterned Superslippery Performance of P-LIGPs.

In situ electrothermal-driven controlled wettability was regarded as a promising method to realize dynamically manipulation and adjust the mobility of droplets on the surface. Additionally, the paraffin-infused interface provided by the porous LIGP could reversibly transit between slippery and nonslippery state with highly switched efficiency. Based on the diversity of *in situ* Joule heating characteristics and differences in sheet resistance, we prepared variety specific pathways for controlling the liquid droplet directional movement. On the basis of our previous study, we systemically studied the patternable electrothermal performance of LIGP heaters by nonuniform laser processing. For the series circuit LIGP regions, its surface temperature is positively related to the resistance.[45] Inspired by the nonuniform temperature distributions, we developed different temperature patterns to achieve programmable wettability for the droplet manipulation, straight, oblique, arc, and S-shaped pathways, which were used for 30 μL liquid droplet directional transportation at a tilt angle of 10° (Figure 5 and Video S4). Notably, pathways were processed at 0.75 W, and other areas were processed at 2.0 W to obtain the larger temperature difference based on Ohm's law and Kirchhoff's laws, which ensured that only paraffin covered on pathways melted. As we can see from Figure 5a, when turning on the input, paraffin films on pathways melted rapidly, and a water droplet slid down quickly from the top of LIGP according to the established designed route in 5 s. The droplet on unmelted areas always had a pinned state. Additionally, Figure 5b–d reveals that other shaped pathways demonstrated programmable wettability, including straight, oblique, arc, and S-shaped pathways. All the droplets had sliding behavior according to the designed route from the top to the end of established pathways. Additionally, we designed and fabricated multifunctional programmable pathways to meet the gradually developing complex microfluidic systems and droplet manipulation technology demands. Figure 5e–g and Video S5 further illustrate that LIGP with complicated V-shaped and arc-straight composite pathways could also be successfully programmed, especially for the V-shaped pathway, which was used for microchemical reactions at a specific location. As Figure 5e, under the input power 4.6 W, paraffin on arc-straight composite pathways melted to obtain the selective superslippery surface, then droplet directional slid from the designed pathways pass about 5 s. Comparatively, droplets on an unmelted area always had a pinned state, which suggested that the unique programmable superslippery surface was successfully fabricated, with the prominent lubricating performance. Additionally, a V-shaped pathway was used for triggering a microreaction at a specific location. As Figure 5f and g, the transparent droplet NaOH and phenolphthalein slid down from the top of the V-shaped pathway and changed to a composite purple droplet after contact with each other at the end of the channel at the input power of 4.5 W. Remarkably, the various programmable pathway-based LIGP is highly promising for a wide range of applications, especially for droplet manipulations and microreactions, exhibiting great potential for future microfluidic systems and laboratory-on-a-chip settings.

Besides the various shaped pathways, we further achieved the sequential "pinned–slide–pinned" behavior by *in situ* regular charging and discharging. With regard to the water droplet (15 μL) on P-LIGP (100 mm × 30 mm) with a tilt angle of 10°, its unique "pinned–slide–pinned" behavior could be easily programmed by *in situ* loading and unloading Joule heat (Figure 6a and Video S6). We further verified the ability to manipulate the droplet motion when the P-LIGP was bent or twisted to a 3D surface. P-LIGP exhibited controllable programmable wettability because of its good flexibility (Figure 6b, c). Therefore, the *in situ* loading and unloading Joule heat could be applied for lighting and extinguishing LEDs by a homemade electric circuit (Figure 6d and Video S7). Once the voltage (12 V) was applied, the saturated NaCl droplet (20 μL) slid down and connected two symmetric copper-wire electrodes within 6 s to light the LED, and the LED extinguished when the droplet skimmed through the electrodes. As shown in Video S8, when *in situ* Joule heat was applied, a water droplet (20 μL) slid over the melted P-LIGP surface. Once the input was cut off, the water droplet stopped within 1 s and continued to slide on the slippery 3D surface when the *in situ* Joule heat was applied again.

During practical usage, the smart P-LIGP inevitably experiences abrasion or scratching that compromises its slippery performance. Therefore, the P-LIGP demonstrates remarkable *in situ* self-healing capabilities. Inspired by the self-healing process of SLIPS,[51] the as-prepared P-LIGP surface also exhibited excellent self-healing properties similar to SLIPS by the localized Joule heating (Figure 7a). As shown in Figure 7b and c, when the slippery surface of P-LIGP was scraped with a knife, a deep damage notch could be detected on the surface, which prevented the water droplets (20 μL) from sliding. When *in situ* Joule heat was applied, the melting paraffin could rapidly flow toward the notch within 10 s through the capillary effect and form a smooth liquid layer on the surface (Figure 7d and Video S9). After the *in situ* unloading of Joule heat, the liquid paraffin solidified and the surface self-healed completely to allow the passage of a water droplet (20 μL) (Figure 7e). This *in situ* self-healing property was also demonstrated by optical microscopic images (Figure 7f–i).

4. CONCLUSION

In summary, LIGPs with porous structures and excellent Joule heating characteristics were successfully used for infusing solid paraffin and applied for fabricating a responsive superslippery surface. Specifically, LIGP-0.75 W with the lowest surface roughness and largest specific surface area had the optimal superslippery performance (tilt angle ~ 10°, WSA < 8°, moving

https://doi.org/10.1021/acsami.5c04045
ACS Appl. Mater. Interfaces XXXX, XXX, XXX–XXX

velocity ~ 7.14 mm/s) for a 50 μL droplet. Furthermore, P-LIGP could maintain consistent responsive wettability even through 120 repeated bending, rubbing, damaging, heating, and rotating cycles. Moreover, various shaped pathways including straight, oblique, arc, S/V-shaped, and composite pathways with the programmable superslippery property are achieved based on Ohm's law and Kirchhoff's laws, and enabled droplet manipulation and microreaction on particular locations. It is anticipated that LIGP-based superslippery surfaces could be innovatively applied in microfluidic systems for droplet transportation and microreaction manipulation technologies.

■ ASSOCIATED CONTENT

Supporting Information

The Supporting Information is available free of charge at https://pubs.acs.org/doi/10.1021/acsami.5c04045.

BET of P-LIGP, durability test of P-LIGP-1.0W, Raman spectra of LIPG, temperature curves at different widths of P-LIGP(PDF)

Video S1: video of dynamic process of paraffin (MP4)

Video S2: video of sliding behavior at different temperatures (MP4)

Video S3: video of sliding behavior at different power (MP4)

Video S4: video of single paths (MP4)

Video S5: video of composite paths (MP4)

Video S6: *in situ* loading and unloading of Joule heat of paraffin (MP4)

Video S7: lighting and extinguishing LEDs by a homemade electric circuit (MP4)

Video S8: *in situ* loading and unloading of Joule heat of paraffin (MP4)

Video S9: self-healing process of paraffin (MP4)

■ AUTHOR INFORMATION

Corresponding Authors

Sida Luo − *School of Mechanical Engineering and Automation, Beihang University, Beijing 100191, China;* orcid.org/0000-0002-5673-6100; Email: s.luo@buaa.edu.cn

Mingguang Han − *School of Mechanical Engineering and Automation, Beihang University, Beijing 100191, China*; Email: mingguang@buaa.edu.cn

Xiao Wu − *Aviation Key Lab of Science and Technology on High Performance Electromagnetic Windows, AVIC Research Institute for Special Structures of Aeronautical Composite, Jinan 250023, China*; Email: 15600624485@163.com

Authors

Yanan Wang − *Aviation Key Lab of Science and Technology on High Performance Electromagnetic Windows, AVIC Research Institute for Special Structures of Aeronautical Composite, Jinan 250023, China*

Pingping Hao − *School of Mechanical Engineering and Automation, Beihang University, Beijing 100191, China*

Yan Gao − *Centre for Advanced Laser Manufacturing (CALM), School of Mechanical Engineering, Shandong University of Technology, Zibo 255000, China*

Mengchen Sun − *Aviation Key Lab of Science and Technology on High Performance Electromagnetic Windows, AVIC Research Institute for Special Structures of Aeronautical Composite, Jinan 250023, China*

Complete contact information is available at: https://pubs.acs.org/10.1021/acsami.5c04045

Author Contributions

[‖]Y. Wang and P. Hao contributed equally to this work.

Notes

The authors declare no competing financial interest.

■ ACKNOWLEDGMENTS

S.L. gratefully acknowledges AVIC Research Institute for Special Structures of Aeronautical Composite for funding this research. This work was also jointly supported by National Natural Science Foundation of China (Nos. 62371025 and T2121003), China Postdoctoral Science Foundation (Nos. BX20240460 and 2024M764079), Beijing Natural Science Foundation (No. 3202017), and Shandong Provincial Natural Science Foundation (No. ZR2023QF022).

■ REFERENCES

(1) Paulssen, D.; Hardt, S.; Levkin, P. A. Droplet Sorting and Manipulation on Patterned Two-Phase Slippery Lubricant-Infused Surface. *ACS Appl. Mater. Interfaces* **2019**, *11* (17), 16130−16138.

(2) Li, J.; Ueda, E.; Paulssen, D.; Levkin, P. A. Slippery Lubricant-Infused Surfaces: Properties and Emerging Applications. *Adv. Funct. Mater.* **2019**, *29* (4), 1802317−1802330.

(3) Wang, Z.; Peng, S.; Wu, L.; Weng, Z. Construction of ultra-long service life self-cleaning slippery surface on superhydrophobicity functionalized by ATRP treatment. *Chem. Eng. J.* **2022**, *428*, 130997−131007.

(4) Tesler, A. B.; Sheng, Z.; Lv, W.; Fan, Y.; Fricke, D.; Park, K. C.; Alvarenga, J.; Aizenberg, J.; Hou, X. Metallic Liquid Gating Membranes. *ACS Nano* **2020**, *14* (2), 2465−2474.

(5) Amini, S.; Kolle, S.; Petrone, L.; Ahanotu, O.; Sunny, S.; Sutanto, C. N.; Hoon, S.; Cohen, L.; Weaver, J. C.; Aizenberg, J.; Vogel, N.; Miserez, A. Preventing mussel adhesion using lubricant-infused materials. *Science* **2017**, *357* (6352), 668−673.

(6) Tesler, A. B.; Prado, L. H.; Khusniyarov, M. M.; Thievessen, I.; Mazare, A.; Fischer, L.; Virtanen, S.; Goldmann, W. H.; Schmuki, P. A One-Pot Universal Approach to Fabricate Lubricant-Infused Slippery Surfaces on Solid Substrates. *Adv. Funct. Mater.* **2021**, *31* (27), 2101090−2101106.

(7) Yu, P.; Lian, Z.; Xu, J.; Yu, H. Slippery liquid infused porous surfaces with corrosion resistance potential on aluminum alloy. *RSC Adv.* **2021**, *11* (2), 847−855.

(8) Yu, Y.; Jin, B.; Jamil, M. I.; Cheng, D.; Zhang, Q.; Zhan, X.; Chen, F. Highly Stable Amphiphilic Organogel with Exceptional Anti-icing Performance. *ACS Appl. Mater. Interfaces* **2019**, *11* (13), 12838−12845.

(9) Wong, W. S. Y.; Hegner, K. I.; Donadei, V.; Hauer, L.; Naga, A.; Vollmer, D. Capillary Balancing: Designing Frost-Resistant Lubricant-Infused Surfaces. *Nano Lett.* **2020**, *20* (12), 8508−8515.

(10) Rao, Q.; Tong, Z.; Song, L.; Ali, A.; Hou, Y.; He, Q.; Lu, J.; Gao, X.; Zhan, X.; Zhang, Q. NIR-driven fast construction of patterned-wettability on slippery lubricant infused surface for droplet manipulation. *Chem. Eng. J.* **2022**, *428*, 131141−131152.

(11) Zhang, J.-R.; Li, A.; Sun, Z.-J.; Wang, Q.; Zhang, Y.-L.; Han, D.-D. High linearity and low hysteresis LMPs/MXene/AgNWs strain sensor for human motion detection. *Appl. Phys. Lett.* **2025**, *126* (3), 033505.

(12) Qin, Y.; She, P.; Wong, W.-Y. Recent advances in dynamically photo-responsive metal complexes for optoelectronic applications. *Innovation Mater.* **2024**, *2* (4), 100099.

(13) Tian, J.; Cao, W. Reconfigurable flexible metasurfaces: from fundamentals towards biomedical applications. *PhotoniX* **2024**, *5* (1), 2.

(14) Rao, C.; Zhong, L.; Guo, Y.; Li, M.; Zhang, L.; Wei, K. Astronomical adaptive optics: a review. *PhotoniX* **2024**, *5* (1), 16.

(15) Jiao, Z.; Hu, Z.; Shi, Y.; Xu, K.; Lin, F.; Zhu, P.; Tang, W.; Zhong, Y.; Yang, H.; Zou, J. Reprogrammable, intelligent soft origami LEGO coupling actuation, computation, and sensing. *Innovation* **2024**, *5* (1), 100549.
(16) Yao, X.; Hu, Y.; Grinthal, A.; Wong, T. S.; Mahadevan, L.; Aizenberg, J. Adaptive fluid-infused porous films with tunable transparency and wettability. *Nat. Mater.* **2013**, *12* (6), 529−534.
(17) Huang, Y.; Stogin, B. B.; Sun, N.; Wang, J.; Yang, S.; Wong, T. S. A Switchable Cross-Species Liquid Repellent Surface. *Adv. Mater.* **2017**, *29* (8), 1604641−1604648.
(18) Wang, Z.; Heng, L.; Jiang, L. Effect of lubricant viscosity on the self-healing properties and electrically driven sliding of droplets on anisotropic slippery surfaces. *J. Mater. Chem. A* **2018**, *6* (8), 3414−3421.
(19) Long, Y.; Yin, X.; Mu, P.; Wang, Q.; Hu, J.; Li, J. Slippery liquid-infused porous surface (SLIPS) with superior liquid repellency, anti-corrosion, anti-icing and intensified durability for protecting substrates. *Chem. Eng. J.* **2020**, *401*, 126137−126146.
(20) Yuan, S.; Peng, J.; Zhang, X.; Lin, D.; Geng, H.; Han, B.; Zhang, M.; Wang, H. A mechanically robust slippery surface with 'corn-like' structures fabricated by in-situ growth of TiO2 on attapulgite. *Chem. Eng. J.* **2021**, *415*, 128953−128967.
(21) Li, Q.; Guo, Z. Lubricant-infused slippery surfaces: Facile fabrication, unique liquid repellence and antireflective properties. *J. Colloid Interface Sci.* **2019**, *536*, 507−515.
(22) Sunny, S.; Vogel, N.; Howell, C.; Vu, T. L.; Aizenberg, J. Lubricant-Infused Nanoparticulate Coatings Assembled by Layer-by-Layer Deposition. *Adv. Funct. Mater.* **2014**, *24* (42), 6658−6667.
(23) Liang, J.; Bian, H.; Yang, Q.; Fang, Y.; Shan, C.; Bai, X.; Cheng, Y.; Yong, J.; Hou, X.; Chen, F. Femtosecond laser-patterned slippery surfaces on PET for liquid patterning and blood resistance. *Opt. Laser Technol.* **2020**, *132*, 106469−106475.
(24) Yong, J.; Huo, J.; Yang, Q.; Chen, F.; Fang, Y.; Wu, X.; Liu, L.; Lu, X.; Zhang, J.; Hou, X. Femtosecond Laser Direct Writing of Porous Network Microstructures for Fabricating Super-Slippery Surfaces with Excellent Liquid Repellence and Anti-Cell Proliferation. *Adv. Mater. Interfaces* **2018**, *5* (7), 1701479−1701488.
(25) Zhang, X.; Wu, G.; Peng, X.; Li, L.; Feng, H.; Gao, B.; Huo, K.; Chu, P. K. Mitigation of Corrosion on Magnesium Alloy by Predesigned Surface Corrosion. *Sci. Rep.* **2015**, *5*, 17399−17400.
(26) Zeng, R.-C.; Liu, Z.-G.; Zhang, F.; Li, S.-Q.; Cui, H.-Z.; Han, E.-H. Corrosion of molybdate intercalated hydrotalcite coating on AZ31 Mg alloy. *J. Mater. Chem. A* **2014**, *2* (32), 13049−13057.
(27) Yousefi, N.; Lu, X.; Elimelech, M.; Tufenkji, N. Environmental performance of graphene-based 3D macrostructures. *Nat. Nanotechnol.* **2019**, *14* (2), 107−119.
(28) Yu, X.; Cheng, H.; Zhang, M.; Zhao, Y.; Qu, L.; Shi, G. Graphene-based smart materials. *Nat. Rev. Mater.* **2017**, *2* (9), 17064−17077.
(29) Papageorgiou, D. G.; Kinloch, I. A.; Young, R. J. Mechanical properties of graphene and graphene-based nanocomposites. *PROG MATER SCI* **2017**, *90*, 75−127.
(30) Mao, J. W.; Han, D. D.; Zhou, H.; Sun, H. B.; Zhang, Y. L. Bioinspired Superhydrophobic Swimming Robots with Embedded Microfluidic Networks and Photothermal Switch for Controllable Marangoni Propulsion. *Adv. Funct. Mater.* **2023**, *33* (6), 2208677.
(31) Han, D.-D.; Chen, Z.-D.; Li, J.-C.; Mao, J.-W.; Jiao, Z.-Z.; Wang, W.; Zhang, W.; Zhang, Y.-L.; Sun, H.-B. Airflow Enhanced Solar Evaporation Based on Janus Graphene Membranes with Stable Interfacial Floatability. *ACS Appl. Mater. Interfaces* **2020**, *12* (22), 25435−25443.
(32) Zhang, Y. L.; Liu, Y. Q.; Han, D. D.; Ma, J. N.; Wang, D.; Li, X. B.; Sun, H. B. Quantum-Confined-Superfluidics-Enabled Moisture Actuation Based on Unilaterally Structured Graphene Oxide Papers. *Adv. Mater.* **2019**, *31* (32), 1901585.
(33) Han, D.-D.; Zhang, Y.-L.; Chen, Z.-D.; Li, J.-C.; Ma, J.-N.; Mao, J.-W.; Zhou, H.; Sun, H.-B. Carnivorous plants inspired shape-morphing slippery surfaces. *OPTO-ELECTRON ADV* **2023**, *6* (1), 210163−210163.
(34) Zhang, Y.-L.; Ma, J.-N.; Liu, S.; Han, D.-D.; Liu, Y.-Q.; Chen, Z.-D.; Mao, J.-W.; Sun, H.-B. A "Yin"-"Yang" complementarity strategy for design and fabrication of dual-responsive bimorph actuators. *NANO ENERGY* **2020**, *68*, 104302.
(35) Wang, J.; Gao, W.; Zhang, H.; Zou, M.; Chen, Y.; Zhao, Y. Programmable wettability on photocontrolled graphene film. *Sci. Adv.* **2018**, *4* (9), 7392−7398.
(36) Wang, J.; Sun, L.; Zou, M.; Gao, W.; Liu, C.; Shang, L.; Gu, Z.; Zhao, Y. Bioinspired shape-memory graphene film with tunable wettability. *Sci. Adv.* **2017**, *3* (6), 1700004−1700011.
(37) Wang, Y.; Wang, Y.; Zhang, P.; Liu, F.; Luo, S. Laser-Induced Freestanding Graphene Papers: A New Route of Scalable Fabrication with Tunable Morphologies and Properties for Multifunctional Devices and Structures. *Small* **2018**, *14* (36), 1802350−1802359.
(38) Liu, F.; Li, L.; Wang, G.; Wang, D.; Ding, X.; Luo, S. Combined extrusion-printed and laser-induced graphene enabled self-sensing composites with a strategic roadmap toward optimization of piezoresistivity. *COMPOS PART A: APPL SCI MANUF* **2021**, *149*, 106553−106563.
(39) Chen, J.; Wang, Y.; Liu, F.; Luo, S. Laser-Induced Graphene Paper Heaters with Multimodally Patternable Electrothermal Performance for Low-Energy Manufacturing of Composites. *ACS Appl. Mater. Interfaces* **2020**, *12* (20), 23284−23297.
(40) Singh, S. P.; Li, Y.; Be'er, A.; Oren, Y.; Tour, J. M.; Arnusch, C. J. Laser-Induced Graphene Layers and Electrodes Prevents Microbial Fouling and Exerts Antimicrobial Action. *ACS Appl. Mater. Interfaces* **2017**, *9* (21), 18238−18247.
(41) Niu, Y.; Sun, Y.; Tao, X.; Liao, C.; Yao, J. Superhydrophobic-electrothermal laser-induced graphene for effectively anti-icing and de-icing. *COMPOS COMMUN* **2024**, *46*, 101830.
(42) Wang, L.; Hu, J.; Zhou, X.; Liu, M.; Wu, Y.; Zheng, H. Modification-free bionic superhydrophobic laser-induced graphene (LIG) wearable strain sensor with superior anti-icing performance. *Chem. Eng. J.* **2025**, *508*, 161140.
(43) Wang, L.; Yin, K.; Deng, Q.; Huang, Q.; Arnusch, C. J. Multiscale hybrid-structured femtosecond laser-induced graphene with outstanding photo-electro-thermal effects for all-day anti-icing/deicing. *Carbon* **2024**, *219*, 118824.
(44) Cheng, L.; Yeung, C. S.; Huang, L.; Ye, G.; Yan, J.; Li, W.; Yiu, C.; Chen, F.-R.; Shen, H.; Tang, B. Z.; Ren, Y.; Yu, X.; Ye, R. Flash healing of laser-induced graphene. *Nat. Commun.* **2024**, *15* (1), 2925.
(45) He, M.; Wang, G.; Zhu, Y.; Wang, Y.; Liu, F.; Luo, S. In-situ joule heating-triggered nanopores generation in laser-induced graphene papers for capacitive enhancement. *Carbon* **2022**, *186*, 215−226.
(46) Bobinger, M. R.; Romero, F. J.; Salinas-Castillo, A.; Becherer, M.; Lugli, P.; Morales, D. P.; Rodríguez, N.; Rivadeneyra, A. Flexible and robust laser-induced graphene heaters photothermally scribed on bare polyimide substrates. *Carbon* **2019**, *144*, 116−126.
(47) Chen, C.; Zhou, L.; Shi, L. A.; Zhu, S.; Huang, Z.; Xue, C.; Li, J.; Hu, Y.; Wu, D.; Chu, J. Ultralow-Voltage-Driven Smart Control of Diverse Drop's Anisotropic Sliding by in Situ Switching Joule Heat on Paraffin-Infused Microgrooved Slippery Surface. *ACS Appl. Mater. Interfaces* **2020**, *12* (1), 1895−1904.
(48) Gao, W.; Wang, J.; Zhang, X.; Sun, L.; Chen, Y.; Zhao, Y. Electric-tunable wettability on a paraffin-infused slippery pattern surface. *Chem. Eng. J.* **2020**, *381*, 122612−122618.
(49) Luo, S.; Hoang, P. T.; Liu, T. Direct laser writing for creating porous graphitic structures and their use for flexible and highly sensitive sensor and sensor arrays. *Carbon* **2016**, *96*, 522−531.
(50) Jia, W.; Yang, S.; Ren, S.; Ma, L.; Wang, J. Preparation and tribological behaviors of porous oil-containing polyimide/hollow mesoporous silica nanospheres composite films. *TRIBOL INT* **2020**, *145*, 106184−106192.
(51) Wong, T. S.; Kang, S. H.; Tang, S. K.; Smythe, E. J.; Hatton, B. D.; Grinthal, A.; Aizenberg, J. Bioinspired self-repairing slippery surfaces with pressure-stable omniphobicity. *Nature* **2011**, *477* (7365), 443−447.

https://doi.org/10.1021/acsami.5c04045
ACS Appl. Mater. Interfaces XXXX, XXX, XXX−XXX